Applications of Thermographic Particle Image Velocimetry to Film Cooling Flow Experiments in a Closed Loop Wind Tunnel

Christopher Abram[1,*], Michael Straußwald[2], Tobias Sander[2], Lars Zigan[2], Michael Pfitzner[2]
1: Dept. of Mechanical and Aerospace Engineering, Princeton University, USA
2: Institut für Thermodynamik, Fakultät für Luft- und Raumfahrttechnik,
, Universität der Bundeswehr München, Germany
* Corresponding author: cabram@princeton.edu

Keywords: Phosphor thermometry, Gas turbine film cooling, PIV, Heat transfer, Turbulence, Optical measurements

ABSTRACT

A laser-imaging method based on thermographic phosphor tracer particles (thermographic particle image velocimetry (TPIV)) is used to simultaneously measure temperature and velocity fields in film cooling flows in wind tunnels, in order to compare novel film cooling configurations under conditions of realistic mainstream turbulence. Several important experimental factors that affect the measurement precision, accuracy, and ultimately the success of the technique in its application in these practical environments are identified: (1) the choice of phosphor particles, which affects the inherent temperature sensitivity and flow tracing accuracy; (2) the particle seeding and management of particle deposition, which affects control of the overall particle number density and seeding uniformity and temporal stability; (3) the setup of the excitation laser/detection cameras and the wind tunnel geometry, which influences background interference from deposited particles and potential influence of multiple scattering. This paper discusses these three factors, gathering and adding to information in prior journal publications, to provide guidance and future research directions for experimental researchers wishing to use these optical diagnostics in film cooling studies and similar enclosed geometries.

1. Introduction

Film cooling is a critical gas turbine technology to reduce heat loads on the combustion chamber and the turbine vanes and blades. Two factors drive a continued need for film cooling research and development: First, gas turbine film cooling strategies must provide adequate cooling performance under high levels of mainstream turbulence, wherein detailed information about the structure, dynamics and transport of the cooling films is needed to understand the underlying flow physics. Second, to improve film cooling performance, various cooling configurations, for example a trenched layout where the holes are connected by a cross-stream slot in the surface, have been developed and require investigation and quantitative comparison to existing cooling hole configurations. For these two reasons, non-intrusive measurements of the flow temperature,

velocity, and derived quantities like the turbulent heat flux in well-defined, generic flow configurations must be developed.

We have applied a laser-imaging method based on thermographic phosphor tracer particles (thermographic particle image velocimetry (TPIV), see Abram et al., 2018) to simultaneously measure temperature and velocity fields in film cooling flows in wind tunnels (Abram et al., 2016; Schreivogel et al., 2016), in order to compare novel film cooling configurations under conditions of realistic mainstream turbulence (Straußwald et al., 2021; Straußwald et al., 2022; Straußwald, 2022). In the course of these experimental campaigns, we have identified a number of factors which have a decisive impact on the measurement precision, accuracy, and ultimately therefore the success of the technique in its application in these practical environments. In this paper, we report on these problems and solutions to disclose our findings and provide guidance and future research directions for experimental researchers wishing to use these optical diagnostics in film cooling studies and similar geometries.

2. Experimental setup

The test rig used is a closed-loop thermal wind tunnel at the Universität der Bundeswehr München (**Fig. *1***).

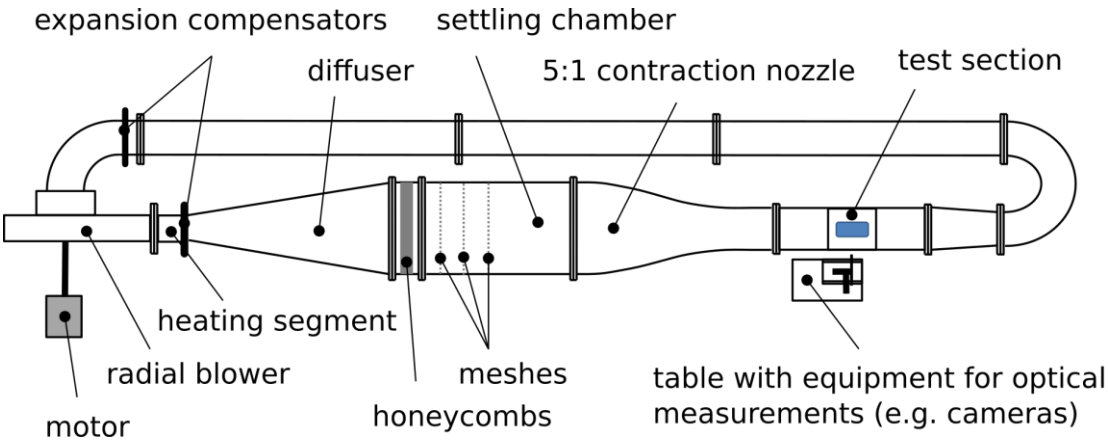

Fig. 1: Schematic of the closed-loop thermal wind tunnel. (Straußwald, 2022)

The flow is driven by a radial blower and flows through a heating segment, a settling chamber and a 5:1 contraction nozzle before entering the test section with a cross-section of 400 mm × 150 mm (width × height). The blower and the heater (P_{el} = 18 kW) are controlled so that the flow has a mean velocity of v_m = 10 m/s and a temperature of up to T_m = 373 K inside the test section. The flow parameters are monitored using a Prandtl probe and a Pt100 resistance thermometer. Optical access is realized through windows on the upper wall and on the front.

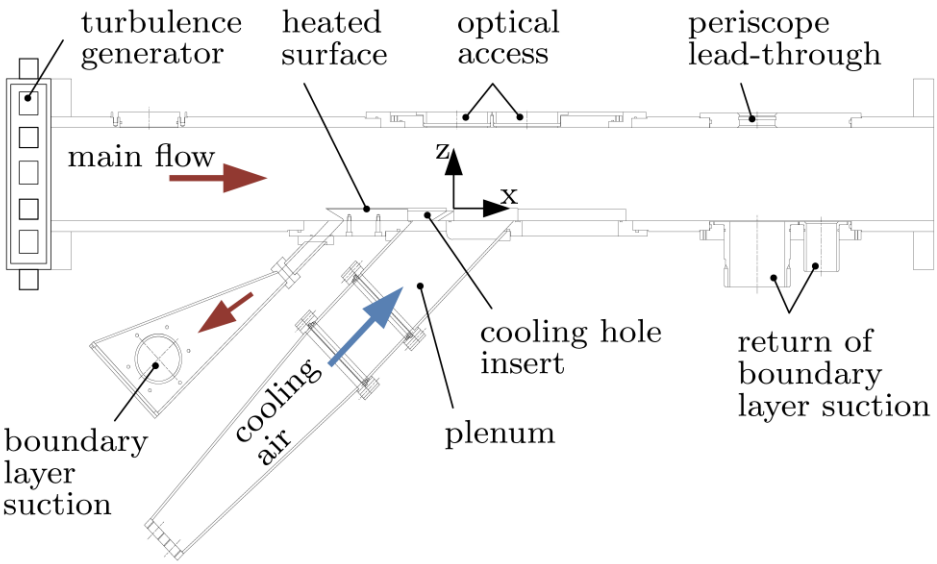

Fig. 2: Sectional view of the measuring chamber of the closed-loop thermal wind tunnel. (Straußwald et al., 2021)

The test plate with a total size of 514 mm × 140 mm (length × width) is located in the center of the test section (**Fig. 2**) and divided into three segments. Upstream of the test plate, the near-wall flow is removed by a boundary layer suction so that a defined turbulent boundary layer can develop on the first test plate segment (length: 140 mm) with the aid of a trip wire, which is placed 80 mm downstream of the leading edge. In addition, a foil heater installed in the first segment creates an adiabatic temperature profile in the wall-normal direction. The cooling air is discharged via the second plate segment (length: 79 mm), whose geometry can be easily interchanged. In this study the geometry consists of a single row with three cylindrical cooling holes (diameter of 6 mm) that are inclined at an angle of 30° (see Straußwald et al. 2021). The cooling air is prepared in a plenum on the underside of the second plate segment and then fed into the holes in the film cooling insert. The last plate segment (length: 295 mm) forms the section of the wall to be cooled, which can also be exchanged, thus enabling various measurement techniques, such as the measurement of surface temperatures or heat transfer coefficients. Downstream of the test plate, the extracted boundary layer is returned into the channel. In the center of the test plate, at the transition from the second to the third plate segment, is the origin of the coordinate system used to study film cooling.

Part of the cooling medium is cooled with liquid nitrogen and a heat exchanger such that the cooling air flow at the cooling hole exit has a temperature of 233 K. Another part of the flow is passed through a particle seeder, where it is seeded with particles needed in the measurement chamber as a tracer for the optical measurement techniques (see Results section). In the plenum, the two partial streams from the heat exchanger and the cooling air seeder are mixed, while in combination with a bypass between the two partial streams, temperature, particle density and

mass flow can be adjusted independently. A second seeder in the return flow of the wind tunnel is used to seed the main flow so that particles are present everywhere in the test section to enable full flow field measurements.

Two turbulence generators (installed between the contraction nozzle and the test section) were applied to increase the turbulence level in the main flow in order to provide mainstream flow conditions representative of gas turbine combustors. The active turbulence grid (ATG) consists of eleven rotating axes, each equipped with diamond-shaped plates. Each axis is driven by an individually controllable motor, which allows the grating to operate with nearly constant blockage of the wind tunnel cross section. Hot-wire and high-speed PIV measurements by Bakhtiari et al. (2018) have shown that turbulence levels as high as Tu = 20% can be generated in the measurement section. The vortex generator (VG) consists of a rotating plate (397 mm × 95 mm) and generates nominal turbulence levels up to Tu = 30% (Strausswald, 2022). As the plate rotates, about 60% of the wind tunnel cross-section is periodically blocked, which chokes the flow and results in a dominant frequency that is twice the rotation rate. While the ATG causes mainly homogeneous turbulence, the VG generates turbulence with a dominant frequency that modulates the average turbulent flow field (Fischer et al. 2022). This allows the experimental simulation of two completely different and for the cooling film relevant turbulent inflow properties. The details of the design of the two turbulence generators can be found in Straußwald et al., 2022.

In the TPIV measurement technique employed here, micrometer-sized thermographic phosphor particles (ZnO) are seeded into the main and cooling flow as tracer using the seeding approach described in section 3.2. The particles are electronically excited by a laser light sheet (355 nm, 6 kHz repetition rate) in a thin plane of the flow (1 mm thick, corresponding to a laser fluence in the test section of 8 mJ/cm^2). The resulting temperature-dependent luminescence emission is detected by two high-speed cameras operating at a 6 kHz framing rate arranged in a beamsplitter configuration and equipped with objective lenses and interference colour filters as shown in the figures later in the paper. The planar temperature field is determined using a two-color ratio-based approach (Abram et al., 2018). Simultaneously, velocity measurements are performed with the same tracer particles using conventional PIV based on Mie scattering from the same particles, using a separate high-speed camera/high-speed laser system. Details of the optics and timing of this system as well as image processing and statistical calculations can be found in Schreivogel et al., 2016, Straußwald et al., 2021 and Straußwald et al., 2022. Further details of the choice of phosphor and geometry of the imaging configuration are detailed in sections 3.1 and 3.3, respectively.

3. Results

3.1 Choice of phosphor particles

First, we consider the choice of phosphor particles, i.e. the luminescent tracer. The inherent temperature sensitivity of the phosphor luminescence, and the rapid temperature and velocity equilibrium between the particles and the gas phase, are both critical to measurement performance. We found that by replacing the previously used tracer $BaMgAl_{10}O_{17}:Eu^{2+}$ (BAM:Eu, see Schreivogel et al., 2016) with ZnO, significant gains in accuracy and precision could be achieved. The fivefold increase in sensitivity (~ 1%/K at 300 K, see **Fig. 3** right) of ZnO due to its pronounced spectral redshift with increasing temperature (see **Fig. 3** top) led to a threefold improvement in the single-shot, single-pixel temperature precision to ± 5 K.

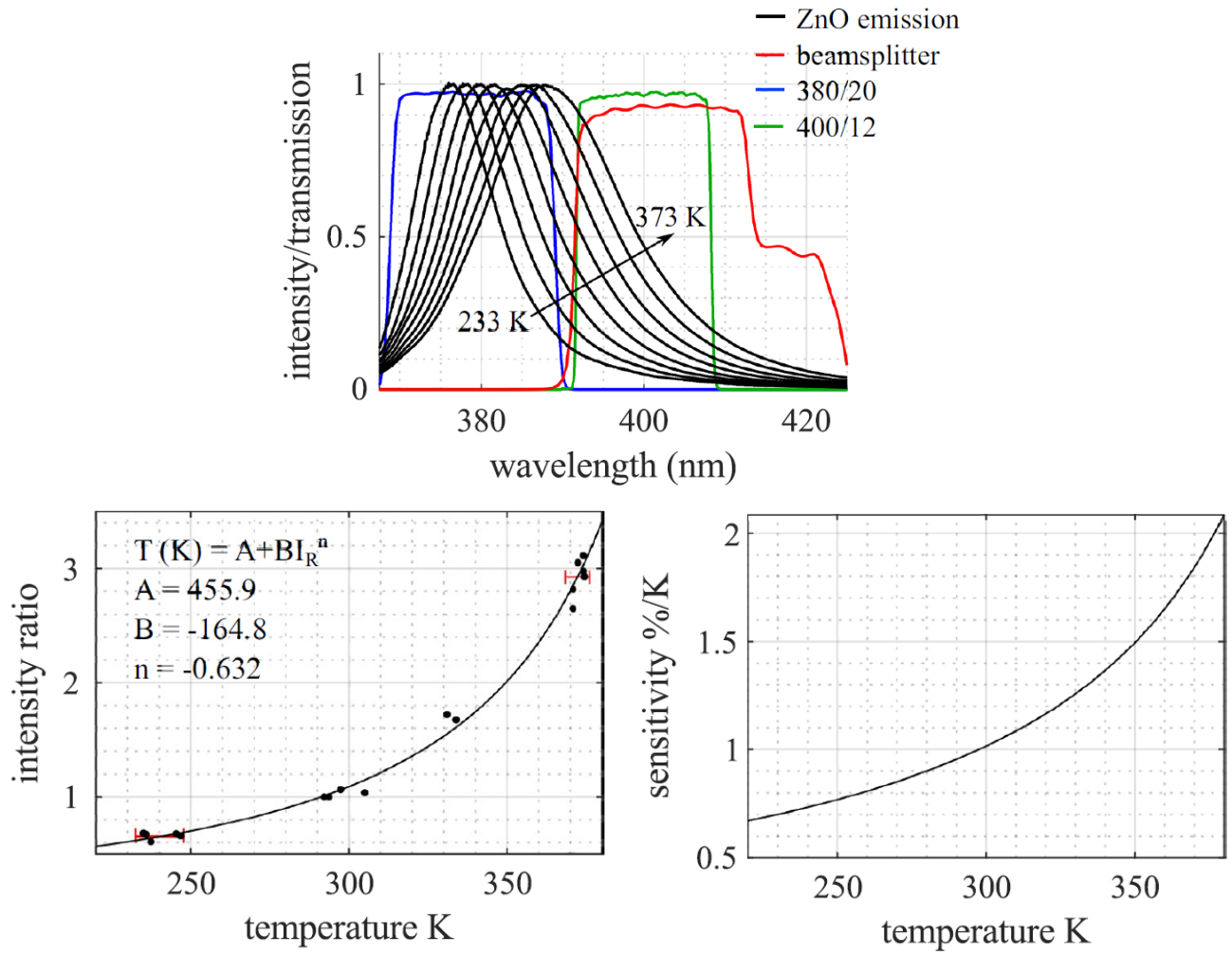

Fig. 3: Top: Temperature-dependent emission spectra for ZnO (normalized) and imaging filters used to isolate the intensity ratio. Bottom: Left: intensity ratio vs. temperature plus fit. Right: derived sensitivity. (Straußwald et al., 2021)

ZnO particles (Sigma-Aldrich, article number 96479) also possess enhanced flow tracing properties due to the smaller particle size (600 nm volume equivalent diameter) and specific morphology of ~ 100 nm primary particles agglomerated into particles ~ 1 µm across (see **Fig. 4**). The relevant response time equivalent sphere-diameter of 380 nm can be calculated from the particle equation of motion in the Stokes regime using the hydraulic diameter (which determines the drag force) and the volume-equivalent diameter (which determines the inertial term), see Fond et al. (2018). Using this diameter, the 95% response time of these particles to a step change in gas temperature or velocity is ~ 5 µs, which represents more than an order of magnitude improvement in response time compared with the previously-used 2.4 µm BAM:Eu particles (Fond et al., 2012). This particle size allows accurate tracking of turbulent fluctuations approaching 10 kHz (Straußwald et al., 2021).

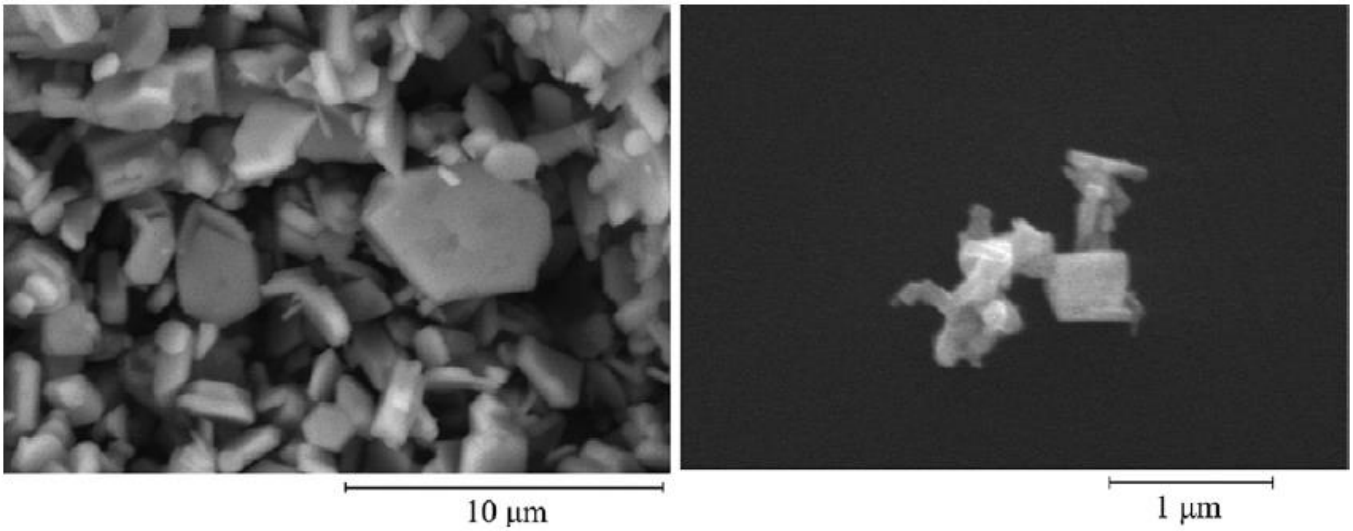

Fig. 4: SEM images of BAM:Eu (left) (Fond et al., 2015) and ZnO particles (right) (Abram et al., 2015).

3.2 Particle seeding and deposition issues

Particle seeding is a practical issue, which required some specific developments to achieve adequate seeding density (in the range 10^{11} particles/m^3 - 10^{12} particles/m^3) in the wind tunnel. We seeded both the main stream and cooling flow independently to acquire measurements everywhere in the flow. For homogeneous main flow seeding various modification steps − including moving the main flow seeding injection location to allow adequate mixing of particles and main flow; adjusting the quantity of particles in the seeder to optimize the particle number density at the measurement location; changing the type of seeder to one specially developed to suit the cohesive particle properties of ZnO particles; and customizing the wind tunnel

components to avoid particle deposition − were necessary, and all required specific development to achieve the right conditions. Furthermore, the ability of rapid 6 kHz acquisition of 18,000 images in 3 s is critical to capture the flow dynamics, but in this regard, we learnt that high-speed measurements are also important to limit the influence of accumulated particle deposition in the test section, which has a major impact on the measurement accuracy adjacent to surfaces.

In particular, the main flow and cooling air seeder are based on a new particle seeder concept, which was developed specifically for seeding of thermographic phosphor particles. This was necessary since we found by experiment that the magnetic-stirrer and cyclone type designs (see Abram et al. (2018)) that were applied with relative ease for BAM:Eu were not suitable when switching to the ZnO phosphor, even when taking steps to ground the seeder and dry the powder prior to use (Straußwald, 2022). In our experiments, ZnO tended to form agglomerates, which results in a sticky bulk of powder inside the seeder compartment that cannot be swirled up to effectively generate a dilute aerosol comprised of non-agglomerated particles. We used a new design (see **Fig. 5**), where to break up the attraction between the particles, the air was fed into the compartment using a wiggling talc-powdered silicone tube. This wiggling action leads to a time-varying and turbulent air flow inside the seeder that impinges on the particle bed in multiple directions, preventing the particles from attaching to walls and breaking up agglomerates.

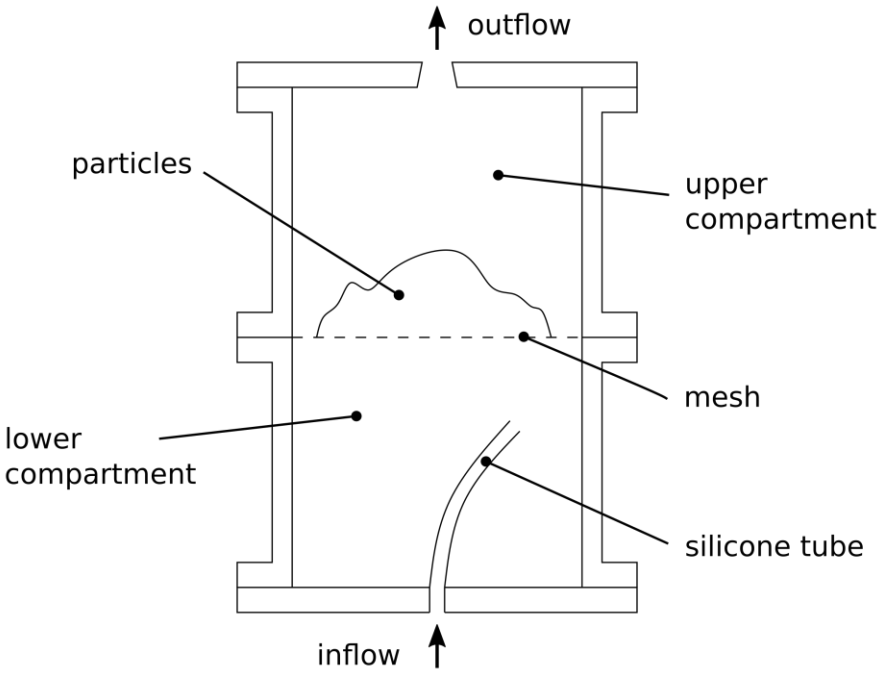

Fig. 5: Schematic of the new seeder design.

Detailed tests on the behavior of the wiggling tube have shown that different shapes of tube motion occur depending on the chosen dimensions of the tube and the volume flow through it. Below a certain volume flow the tube is still and the air enters the seeder at a constant location.

Once the volume flow exceeds this value (transition A) a plane oscillating motion starts and at higher volume flows (transition B) the motion changes to a chaotic wiggling.

Fig. *6* and **Fig. *7*** show transition A and B examples for two different tube geometries. One can see that transition A can be moved to lower volume flows when the volume flow is decreased from higher values. This happens because the oscillating motion is already present and persists, while the tube stays still when the volume flow reaches the same value starting from zero. This hysteresis effect can help to run the seeder even though the operating point has reached the lower limit of the region where the tube starts to oscillate. Furthermore, the data show that transition B starts at a certain level but reaches its fully developed oscillating motion at a higher volume flow. Comparison of different operating points showed that chaotic wiggling provides best results for aerosol generation. This is the case because particle deposition is mainly avoided throughout the seeder compartment. However, plane oscillation was still sufficient to run the thermographic PIV measurements within this setup.

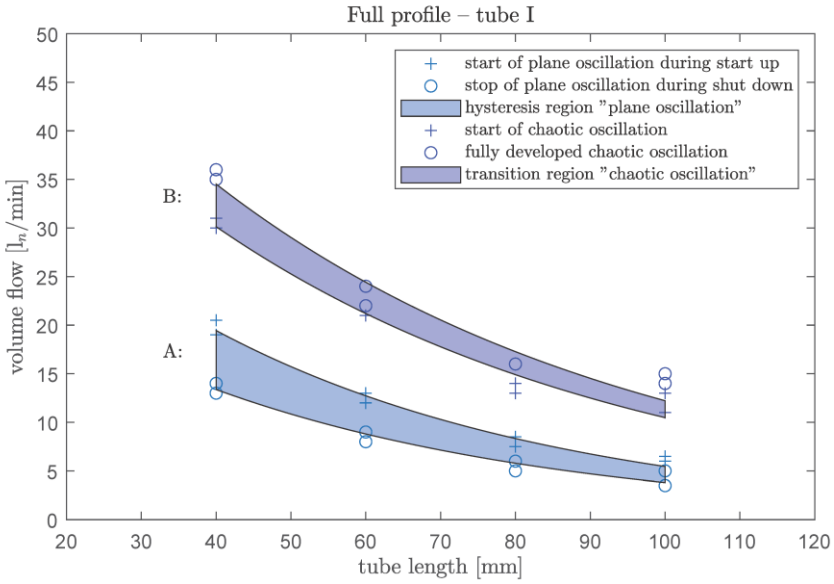

Fig. 6: Transition A and B for a tube with d_i = 1 mm and s = 0.5 mm.

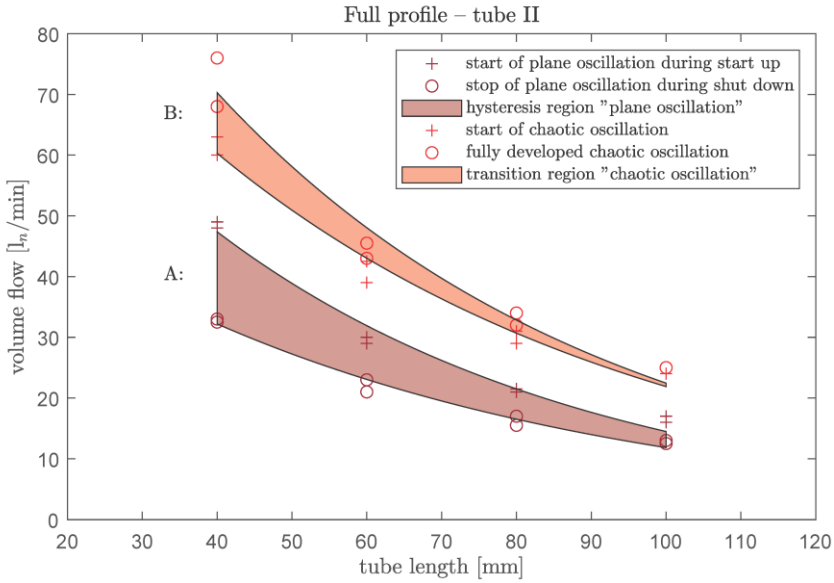

Fig. 7: Transition A and B for a tube with d_i = 1.5mm and s = 0.75 mm.

In case of the cooling air, a relatively small amount of air (below 100 l_n/min) passes through the seeder. In fact, for the intended momentum ratios only 30 l_n/min to 70 l_n/min were necessary to achieve a sufficient seeding density in the final cooling air flow. Therefore, the whole seeder volume flow can go through the wiggling tube, mixes with the particles and enters the plenum before entering the test section through the cooling hole insert. The chosen tube had a length of 70 mm, an inner diameter d_i of 1.5 mm and a wall thickness s of 0.75 mm (tube II). According to **Fig. 7**, this tube covers most of the intended volume flow region with chaotic wiggling. An increased tube length would have improved the performance at low volume flows; however, the available compartment size of the seeder limited the length of the tube.

In case of the main flow, 240 times the volume flow of the cooling air had to be seeded, which led to a slightly different approach. Rather than continuously seeding of the whole wind tunnel flow, a huge number of particles were fed into the wind tunnel within a short period of time. This was realized by splitting the air flow through the main flow seeder into two parts: (1) a small part (again below 100 l_n/min) goes through the wiggling tube swirling up the particles and (2) a larger volume flow that picks up the swirled particles and transports them into the wind tunnel. Applying this approach, up to 80 g of particles could be transported into the wind tunnel within a period as short as 10 seconds, resulting in a homogeneous aerosol by the time the particles had mixed with main flow on their journey around the wind tunnel to the test section. For further information regarding the seeders, the reader is referred to Strausswald, 2022).

Initially, during maintenance of the wind tunnel a huge number of particles were found deposited immediately downstream of the seeding air inlet. The reason was that the wind tunnel seeding flow was fed into the main flow perpendicularly in upwards direction. As a result, the

particle flow impinged the top wall of the wind tunnel and most of the particles fell onto the ground without having the opportunity to mix with the unseeded main flow. Therefore, the seeding air inlet was changed in such way that the aerosol enters the wind tunnel flow in counter flow direction (reverse seeding), which highly improved the mixing process with the main flow. Another issue we found was that particles tend to block the meshes inside the settling chamber (see **Fig. *1***). After previous campaigns, up to 2/3 of the flow cross section was blocked with particles. Therefore, we removed the meshes and checked the homogeneity of the resulting main flow in the measurement chamber. Hot wire data showed a homogeneous flow with a turbulence intensity of $Tu \approx 3$ % (Straußwald, 2022) at the entrance of the test section, which was sufficient for the intended test cases in our latest measurement campaign.

The combination of the described measures led to a reduction of particle usage as a higher percentage of the particles reached the film cooling region. For final measurements, 25 g of ZnO were sufficient such that when dispersed in the huge main flow, the objective of 10^{11} particles/m^3 - 10^{12} particles/m^3 in the measurement plane was reached. Once the seeder operation points were optimized, the amount of main flow seeding was therefore controlled using the mass of particles in the main flow seeder.

Seeding densities were determined using the inverse of a method described in Fond et al. (2015); with the known emission intensity per particle of ZnO and the spectroscopic properties given in Fond et al. (2019) (accounting for laser fluence, gas temperature and excitation wavelength); and the diagnostic setup (including camera quantum efficiency, filter and objective lens transmission, magnification, and light sheet thickness). Using this method, the main flow seeding density is estimated at ~ 2×10^{11} particles/m^3, with a factor 2 higher seeding density in the cooling jet (~ 4×10^{11} particles/m^3) as determined from the Mie scattering intensity.

3.3 Setup modifications - diagnostics and wind tunnel

Various changes to the test section were made to accommodate the diagnostics. When the excitation laser propagates perpendicular to the test plate and impinges directly on it, luminescence from particles deposited on the test plate generated background signals so bright that measurements could not be made adjacent to the surface. Attempts to subtract the background did not work, owing to the changing background signal due to particles deposited during the measurement. Consequently, we employed a periscope design (see **Fig. 8** left), which directed the laser sheet parallel to the surface (Schreivogel et al., 2016). This resulted in orders of magnitude lower excitation fluence for deposited particles, dramatically lowering the background signal and permitting measurements within a few mm of the test plate surface. During operation, the periscope is continuously purged with a gas flow to prevent particles depositing on the lower

turning mirror. We verified using a CFD simulation that this did not influence the film cooling lfow at the measurement location.

Furthermore, we and other investigators previously found that multiple scattering effects in the aerosol by a process such as that depicted in **Fig. 9** left, can lead to systematic temperature errors (Lee et al., 2016). In one prior study using phosphor thermometry with BAM:Eu particles, structured laser illumination planar imaging ("SLIPI") was explored to tackle this issue (Stephan et al., 2019). In this study, we modified the test section to include a bypass, which keeps the cross-sectional area of the cooling flow the same while reducing the amount of seeded air between the measurement plane and the cameras, without changing the film cooling flow itself, see **Fig. 8** right.

Then, to determine if multiple scattering from the large surrounding volume of hot particles influences the cooling flow temperature measurement in this test geometry and using ZnO particles, we performed experiments with and without main flow seeding and compared the resulting intensity ratios (the measurand for temperature), see **Fig. 9** right. The intensity ratio in the marked region of the jet core changed by only ~ 7% when seeding the main flow, a variation which is within the overall uncertainty reflected by the scatter in the calibration data (± 6 K, see **Fig. 3** left). We concluded that multiple scattering effects using ZnO particles in this enclosed wind tunnel geometry at a measured average seeding density of 2×10^{11} particles/m^3 are negligible. The higher absorption of ZnO relative to BAM:Eu leads to similar luminescence signal per particle, but, as discussed above, ZnO particles are smaller than BAM:Eu particles and therefore possess a lower scattering cross-section. For these reasons, for the same seeding density, the ratio of luminescence signal to scattered light can be expected to be higher for ZnO than BAM:Eu. However, further experiments in well-defined geometries are needed to address the reason for this positive result.

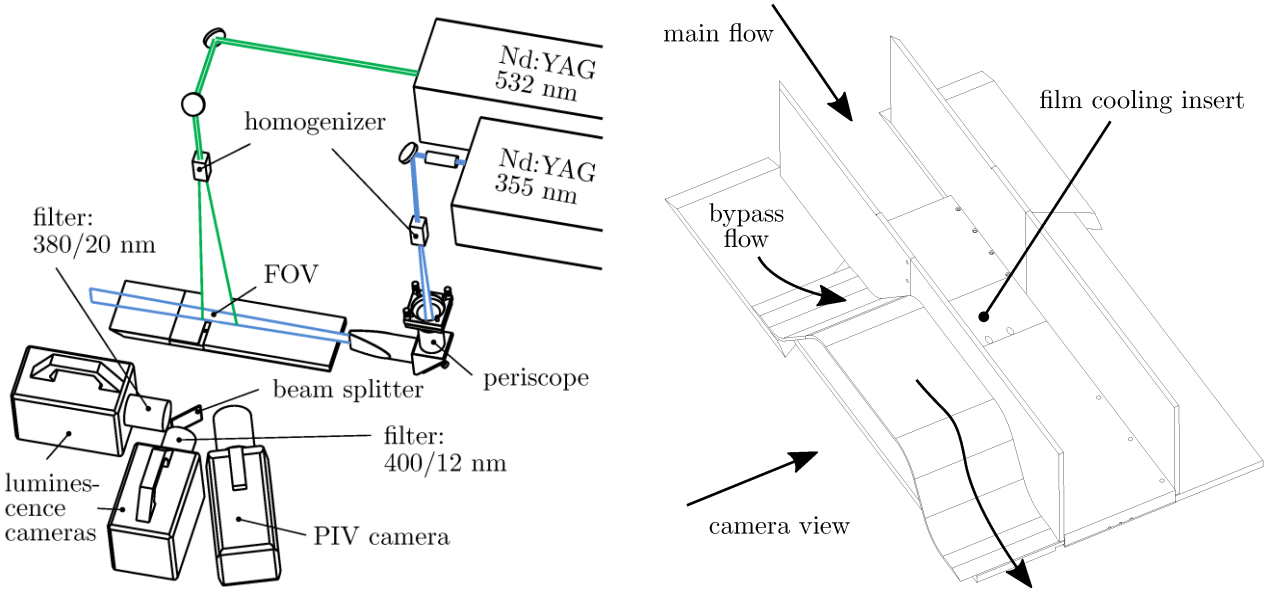

Fig. 8: Left: Thermographic PIV setup, illustrating the periscope design. Right: Installed bypass geometry. (Straußwald et al., 2022)

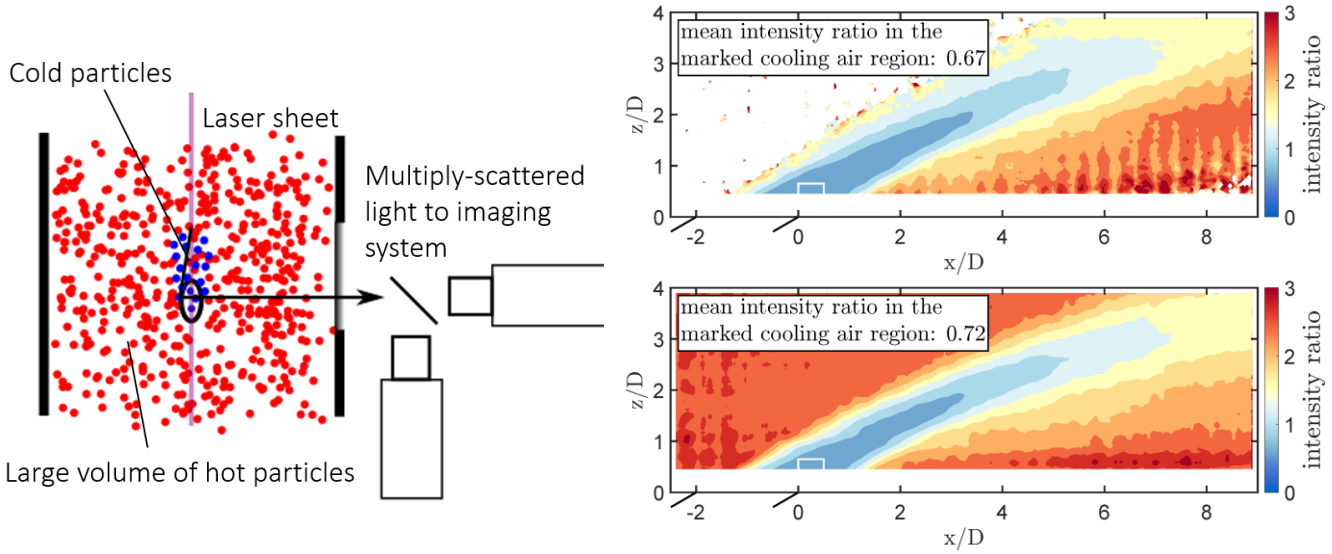

Fig. 9: Left: cartoon of the multiple scattering problem. Right: Time-average intensity ratio field without main flow seeding (upper) and with main flow seeding (lower) at a calculated density of ~ 2×10^{11} particles/m^3 (Straußwald et al., 2021).

3.4 Uncertainty analysis

The mean deviation of the fit to the raw data points recorded for various nominal temperatures on different days of the campaign is ± 6 K (1σ, 4 % of the normalized temperature, see **Fig. 3** left). This value can be taken as the overall uncertainty of these measurements. We have already discussed multiple scattering as a source of systematic error, which could contribute to the overall uncertainty. Here, we also mention laser fluence effects, and uncertainty in the background subtraction.

One drawback of using ZnO tracer particles is that the measured temperature depends on the laser fluence. This is partly due to particle heating and partly due to a genuine photophysical effect at high power densities (Abram et al., 2015). These phenomena can cause measurement errors due to, for example, variation in the laser sheet profile or energy; or attenuation of the laser beam by the particles themselves as the beam propagates in the counter-streamwise direction. The laser power and homogenized sheet profile were extremely stable from shot-to-shot and over the course of the measurement campaign. The seeding system was also relatively repeatable, with only 25 % variation in the time-average Mie scattering signal between the measurement sequences presented here (note this is a measure unaffected by attenuation because the 532 nm light sheet enters the top of the test section and propagates only a short distance through the aerosol). Using the known optical properties of ZnO, and a Mie scattering and absorption calculation (Prahl, 2018),

the attenuation over the ~ 300 mm distance from the periscope to the measurement plane is estimated to be below 10 % at ~ 2×10^{11} particles/m^3. Indeed, we found no correlation between the main flow seeding density (which could change the laser beam attenuation and, therefore, the laser fluence in the test section) and the measured main flow intensity ratio. These facts indicate that, for these experimental conditions of consistent, low-density seeding and stable laser operation, laser fluence effects using ZnO phosphor particles in this configuration are an insignificant source of uncertainty.

A further source of systematic error is background subtraction. The background consists of the CMOS camera offset and also possible interference from particles deposited on the test plate and/or windows during the measurement. The test plate was carefully wiped clean between each measurement sequence. By subtracting time-average background images recorded before and after every measurement sequence from one another, differences below 1 count were identified, which leads to an error commensurate with the scatter in the calibration data in **Fig. 3 left,** and likely dominates the overall inaccuracy.

Besides the accuracy, the random uncertainty (precision), defined as the single-shot, pixel–pixel temperature error as determined from uniform temperature regions of the main flow at 373 K, is ± 5 K (4 % of the normalized temperature, $\theta = 0.04$, see definition below) at 1 mm spatial resolution. Combined with the velocity measurement error (described by Straußwald et al., (2021)), at a frequency of 7 kHz, the turbulent heat flux is underestimated by 6 %. Random and systematic errors are summarized in **Fig. *10***.

Error source	Uncertainty	Notes
Random velocity	~0.5 m/s	–
Tracing error	5%	Underestimate at 7 kHz
Random temperature	±5 K	Determined at 373 K[a]
Systematic temperature	±6 K	[b,a]

[a] ~ 4% of the normalised temperature, $\theta = 0.04$

[b] Includes contributions from all systematic error sources discussed in the text including multiple scattering and background subtraction

Fig. 10: Summary of error sources (± 1σ confidence). (Straußwald et al., 2021)

3.5 Example results

To exemplify the combined experimental improvements described above, we present measurements of temperature, velocity, and derived turbulent heat flux fields in conventional film

cooling flows from 30° inclined cylindrical cooling holes (hole diameter $D = 6\,mm$). An example image is provided in **Fig. *11***. The image shows an instantaneous flow field of cold air emanating from the cooling hole (indicated in the lower left corner of the figure) and a hot cross flow at increased main flow turbulence ($Tu = 16.4\,\%$) produced by the ATG. The momentum ratio (I) between the cold and the hot flow is 3.5 which is calculated from the average temperature and velocity of the two unaffected flows according to $I = (T_c \cdot u_c^2)/(T_m \cdot u_m^2)$. Both, momentum ratio and main flow turbulence, are given in the upper left corner of every image. Colored contours show the normalized temperature field, which is calculated following $\theta = (T_m - T)/(T_m - T_c)$. In addition, the plotted vector field shows the velocity fluctuation, which is calculated by subtracting the average velocity field from 6,000 consecutive images. This form of presenting the velocity was chosen to highlight the turbulences in the incoming main flow and the mixing processes in the shear layers. Further, the white dash-dotted line indicates the central streamline of the average velocity field to allow comparison between average and instantaneous flow field.

The instantaneous snapshot shows a cooling air flow that is lifted off the surface so that hot air can enter the wake region of the jet, resulting in a diminished cooling efficiency. Furthermore, due to the large main flow oscillations, the jet deviates from the average central streamline and mixing in the shear layers is increased. For this reason, the cooling airflow temperature rapidly approaches the temperature of the main flow ($\theta = 0$).

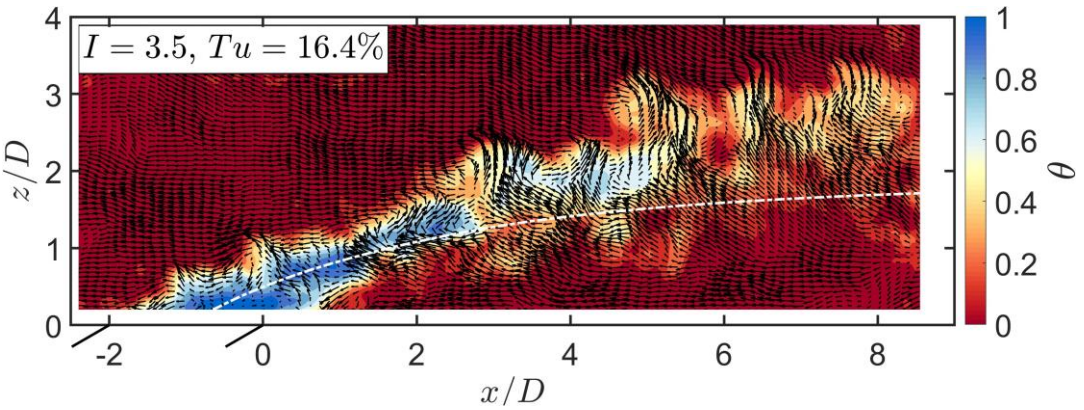

Fig. 11: Sample image showing an instantaneous temperature and velocity fluctuation field for increased main flow turbulence conditions.

Fig. *12* displays the resulting average flow fields at low ($Tu = 5.3\,\%$), medium ($Tu = 16.4\,\%$) and high ($Tu = 22.7\,\%$) main flow turbulence. The low turbulence condition differs from previously mentioned results of the hot wire measurements as now the bypass geometry is installed, and the turbulence intensity is calculated in a region near the cooling air inlet being affected by the bypass. The high turbulence condition is generated with the VG which means that a single oscillation frequency ($f = 5.33\,Hz$) dominates the flow field, while the case with medium turbulence is more

homogeneous as it is generated by the ATG. Comparison of the velocity fields shows only small differences while the temperature distribution clearly varies depending on the test case. At low main flow turbulence, the cold air emanating from the cooling hole reaches the end of the field of view with a normalized temperature of $\theta \approx 0.4$. In case of the ATG flow and $Tu = 16.4$ %, the cold air mixes with the surrounding hot gas leading to $\theta \approx 0.1$ at the end of the field of view. The VG flow, however, shows an expanded cooling jet that seems to perform better compared to the case with the ATG turbulence.

At this point, the advantage of the measurement technique becomes clear. A series of instantaneous temperature-velocity fluctuation fields (e.g. Fig. 13) help to explain the differences in the average flow field for the VG flow ($Tu = 22.7$ %). The presented snapshots (subsampled at a temporal resolution of 2.17 ms, indicated in the upper right corner) show the transformation of the cooling air flow while strong main flow oscillations pass through the field of view. First, the cold air is pushed towards the surface before it almost fully vanishes at $t = 6.5\,ms$. Later, at $t = 8.67\,ms$, the jet starts to recover and reaches its initial spatial dimensions at $t = 15.17\,ms$. This explains the temperature distribution in the average flow field (**Fig. *12***). Rather than representing a real expanded cooling air jet, the jet is temporarily deflected from the average central streamline, which ends up in a false impression of an expanded jet in the average flow field.

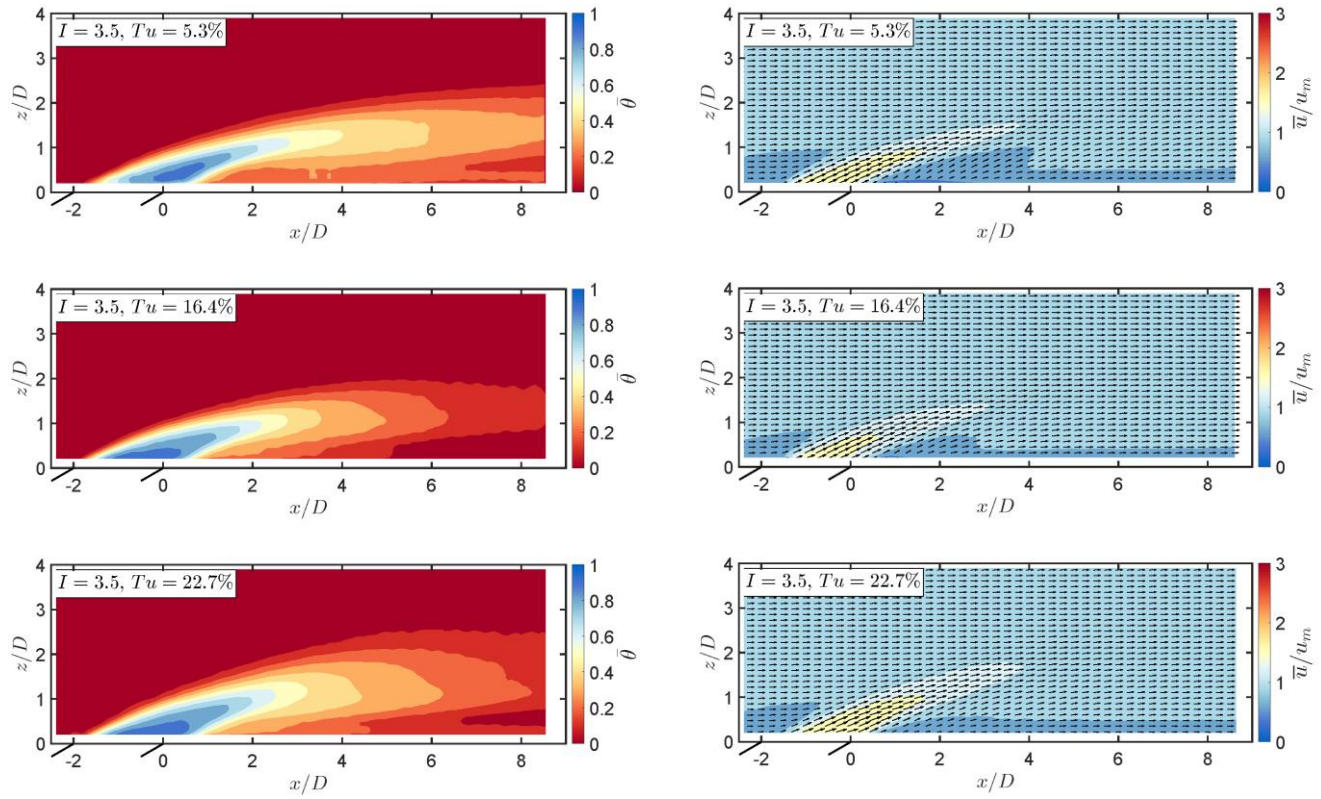

Fig. 12: Comparison of the average temperature (left) and velocity fields (right) for three different main flow turbulence levels.

Another advantage of the gathered data is the possibility to calculate turbulent momentum and turbulent heat flux data. While the turbulent momentum data can be derived from general PIV applications, the turbulent heat flux needs simultaneous measurement of temperature and velocity. Thermographic PIV can provide these data and thus can make a valuable difference in research projects. For instance, the values are typically unknown in RANS (Reynolds Averaged Navier Stokes) simulations and, therefore, measured data are of high interest in modelling and verification of numerical methods. Example values are given in **Fig. *14*** for $I = 3.5$ and $Tu = 5.3$ %. Turbulent heat flux and the turbulent momentum are normalized with $u_m(T_m - T_c)$ and u_m^2, respectively. The turbulent heat flux in z-direction (**Fig. *14*** right) shows negative values in the upper and positive values in the lower shear layer, while the turbulent heat flux in x-direction (**Fig. *14*** left) shows negative values in both shear layers. The latter contradicts the turbulent diffusion hypothesis that is often used in RANS simulations and predicts a positive turbulent heat flux in the upper shear layer in x-direction. Besides the heat flux values, also the location of the shear layers and the potential core can be identified.

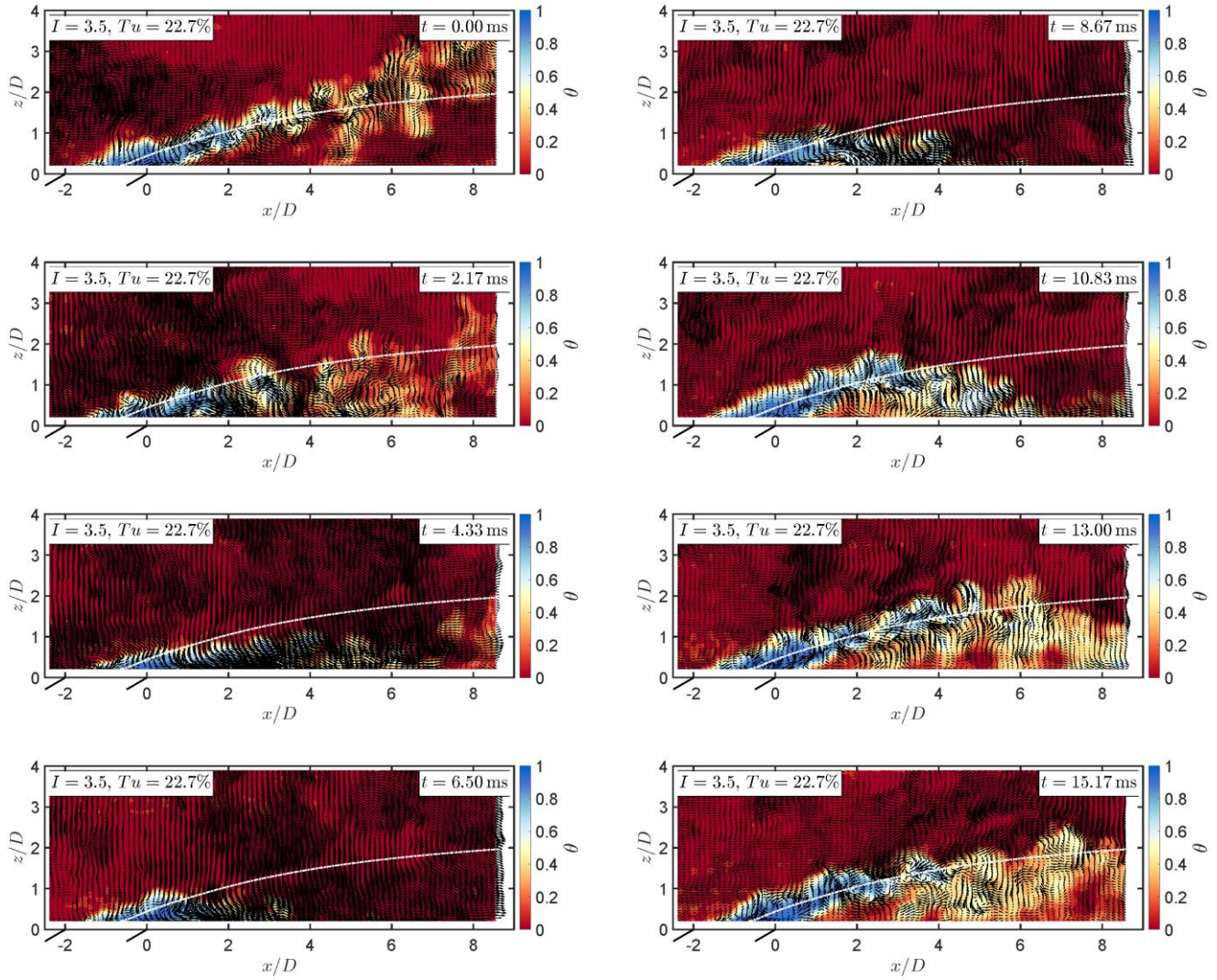

Fig. 13: Series of single shots showing the cooling film being temporarily eliminated due to strong main flow oscillations caused by the vortex generator.

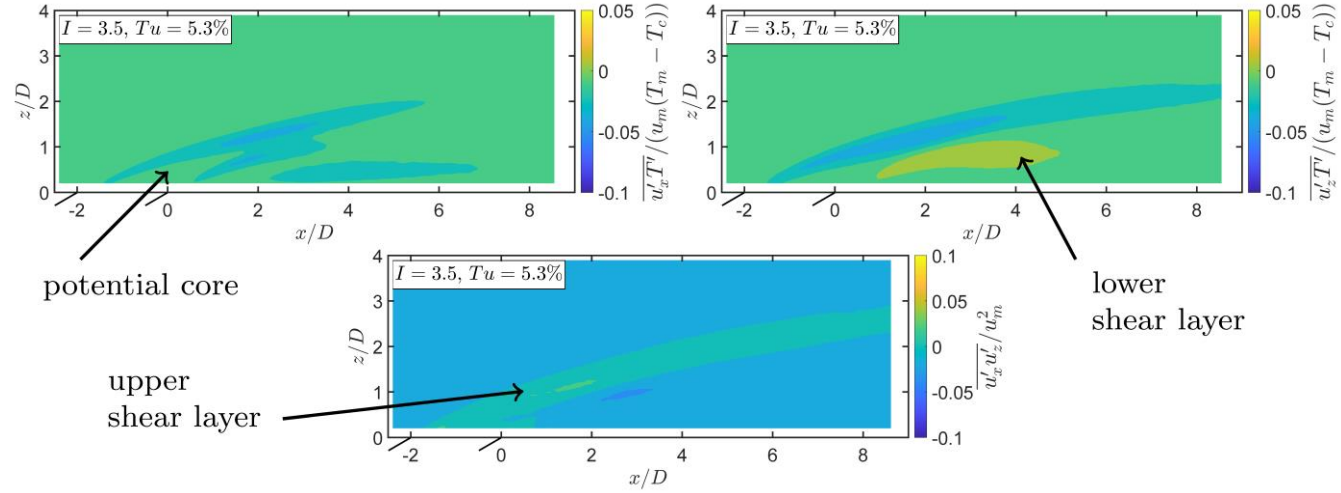

Fig. 14: Turbulent heat flux in x direction (left) and z direction (right), and turbulent momentum (bottom) at low main flow turbulence.

4. Conclusions

The laser-imaging method based on thermographic phosphor tracer particles is applicable to simultaneously measure temperature and velocity fields in film cooling flows in wind tunnels. The method provides temperature and velocity information and insights into the flow physics, and helps the study of novel film cooling configurations under conditions of realistic mainstream turbulence. Several important experimental factors affecting the measurement precision and accuracy were identified: (1) the choice of phosphor particles, (2) the particle seeding and management of particle deposition, (3) the setup of the excitation laser/detection cameras and the specific wind tunnel geometry. With appropriate adjustments, we achieved a temperature sensitivity of 1 %/K using ZnO phosphor particles, improving the single-shot single pixel temperature precision to ± 5 K; and the small (600 nm) size and agglomerate morphology of the particles leads to improved flow tracing. Furthermore, measurements within a few mm of the wall were possible, and no influence of multiple scattering was observed with ZnO particles in the modified geometry at an estimated average seeding density of 3×10^{11} particles/m^3.

In the future, there are two main directions for improving the measurement technique: first, identifying phosphor particles with a yet more temperature-sensitive luminescence emission would improve the measurement accuracy and precision. Second, additional systematic experiments in standard geometries and illumination conditions are needed to improve our understanding of multiple scattering phenomena in the context of fluid thermometry based on luminescent particles, especially in combination with multiple scattering modelling efforts. These two avenues will enable further improvements in the measurement accuracy and precision, and therefore the flexibility for thermometry in other demanding applications.

Acknowledgements

We gratefully acknowledge financial support by the Deutsche Forschungsgemeinschaft (DFG, PF 443/7-1).

References

Abram, C., Fond, B., Beyrau, F. (2015). High-precision flow temperature imaging using ZnO thermographic phosphor tracer particles. *Optics Express*, 23, 19453–19468.

Abram, C., Schreivogel, P., Fond, B., Straußwald, M., Pfitzner, M., Beyrau, F. (2016). Investigation of Film Cooling Flows using Thermographic Particle Image Velocimetry at a 6 kHz Repetition Rate. *Proceedings of the 18th International Symposium on the Application of Laser and Imaging Techniques to Fluid Mechanics*. Lisbon, Portugal, July 4–7.

Abram, C., Fond, B., Beyrau, F. (2018). Temperature measurement techniques for gas and liquid flows using thermographic phosphor tracer particles. *Progress in Energy and Combustion Science*, 64, 93–156.

Bakhtiari, A., Sander, T., Straußwald, M., Pfitzner, M. (2018). Active turbulence generation for film cooling investigations. *Proceedings of ASME Turbo Expo 2018: Turbomachinery Technical Conference and Exposition*, Lillestrøm (Oslo), Norway, GT2018-76451.

Fischer, L., Straußwald, M., Pfitzner, M. (2022). Analysis of LES and 1D hot-wire data to determine actively generated main flow turbulence in a film cooling test rig. *Journal of Turbomachinery*, TURBO-21-1282, accepted for publication.

Fond, B., Abram, C., Heyes, A. L., Kempf, A. M., Beyrau, F. (2012). Simultaneous temperature, mixture fraction and velocity imaging in turbulent flows using thermographic phosphor tracer particles. *Optics Express*, 20, 22118–22133.

Fond, B., Abram, C., Beyrau, F. (2015). Characterisation of the luminescence properties of BAM:Eu^{2+} particles as a tracer for thermographic particle image velocimetry. *Applied Physics B*, 121, 495–509.

Fond, B., Abram, C., Pougin, M., Beyrau, F. (2019). Characterisation of dispersed phosphor particles for quantitative photoluminescence measurements. *Optical Materials*, 89, 615–622.

Lee, H., Böhm, B., Sadiki, A., Dreizler, A. (2016). Turbulent heat flux measurement in a non-reacting round jet, using BAM:Eu^{2+} phosphor thermography and particle image velocimetry. *Applied Physics B,* 122, 1–13.

Prahl, S., (2018). Mie scattering calculator. https ://omlc.org/calc/mie_calc.html. Accessed 4 Oct 2020.

Schreivogel, P., Abram, C., Fond, B., Straußwald, M., Beyrau, F., Pfitzner, M. (2016). Simultaneous kHz-rate temperature and velocity field measurements in the flow emanating from angled and trenched film cooling holes. *International Journal of Heat and Mass Transfer*, 103, 390–400.

Stephan, M., Zentgraf, F., Berrocal, E., Albert, B., Böhm, B., Dreizler, A. (2019). Multiple scattering reduction in instantaneous gas phase phosphor thermometry: applications with dispersed seeding. *Measurement Science and Technology,* 30(5).

Straußwald, M., Abram, C., Sander, T., Pfitzner, M. (2021). Time-resolved temperature and velocity field measurements in gas turbine film cooling flows with mainstream turbulence. *Experiments in Fluids*, 62(3).

Straußwald, M., Sander, T., Abram, C., Pfitzner, M. (2022). Investigating the influence of mainstream turbulence and large vortices on gas turbine trenched film cooling flows using planar temperature-velocity imaging. *Journal of Turbomachinery*, TURBO-21-1260, accepted for publication.

Straußwald, M. (2022). Experimentelle Untersuchung von Filmkühlung unter brennkammertypischen Strömungsbedingungen [Doctoral dissertation, Bundeswehr University Munich]. *Athene Forschung, Bundeswehr University Munich.* https://athene-forschung.unibw.de/141289.